Structurally Constrained Quantitative Susceptibility Mapping

Sara Gharabaghi[1,2], Saifeng Liu[2], Ying Wang[3], Yongsheng Chen[4], Thomas Wischgoll[1], and E. Mark Haacke[2,3,4,5]

[1]Department of Computer Science and Engineering, Wright State University, Dayton, Ohio, 45435, USA, [2]The MRI Institute for Biomedical Research, Bingham Farms, Michigan, USA, [3]SpinTech, Inc., Bingham Farms, Michigan, USA, [4]MRI Innovations, Inc., Bingham Farms, Michigan, USA, [5]Department of Radiology, Wayne State University, Detroit, Michigan, USA.

Introduction: Quantitative susceptibility mapping is a powerful technique that reveals changes in the underlying tissue susceptibility distribution. It is used to study a number of neuro-degenerative diseases since the susceptibility, , is highly correlated with the amount of iron deposition in the tissue (1). Reconstructing from the phase image collected with a gradient echo sequence is an ill-posed inverse problem due to the structure of the dipole kernel. Many approaches have been taken to overcome this difficulty including: thresholding the dipole kernel in the inversion process (TKD (2)), applying a geometrical constraint (iSWIM (3)), and utilizing multiple orientations to stabilize the inversion process (COSMOS (4)). Other studies try to use regularization techniques and different prior information such as structural constraints from magnitude images in the form of -norm (MEDI (5)), or from both magnitude and phase images in the form of -norm (HEIDI (6)). In (7), a structural constrained reconstruction (SFCR) method is proposed that is composed of two separate steps each includes both a fidelity term and two - and -norm regularization terms. In the first step, the initial susceptibility map is reconstructed based on prior magnitude information. In the second step, the susceptibility map is fitted in the spatial domain using a weighted constraint derived from the initial map. The problems with the current QSM reconstruction algorithms are mainly related to the reliability of the geometry constraint and the speed of the reconstruction.

In this study, we proposed a structurally constrained SWIM (SCSWIM) method that is based on the SFCR concept but utilizes the structural information from the both the magnitude image and susceptibility map in a single step. A preconditioned conjugate gradient approach is used that helps it converge quickly. Furthermore, we use prior information about deep gray matter structures and vessels to avoid over-smoothing these structures. The proposed method uses iSWIM data as the initial input since it has enhanced visualization of the vessels. Additionally, we take advantage of the enhanced contrast of STAGE imaging (8), (9) which uses different flip angles in two double-echo sequences to provide a better geometry constraint compared to the conventional GRE.

Methods: The relationship between and phase image can be described as (10):

, [1]

where , , and are the gyromagnetic ratio, main magnetic field, echo time and dipole kernel, respectively. Also, and are the Fourier and inverse Fourier operations. The objective function of SCSWIM that is derived from the second step of SFCR is given as:

[2]

The first term is the data fidelity term where is a weighting matrix proportional to the magnitude that defines the reliability of the magnetic field shift for each voxel. The two regularization terms use the prior structural information of the white matter, gray matter, basal ganglia and vessels. The first regularization term is based on the edge matrix, , which is the binary mask that is derived from the union of the thresholded gradients of the magnitude and the initial susceptibility. We have taken advantage of the improved contrast of the enhanced T1-W STAGE data to extract the edge of the white matter and gray matter (**Figure 1**). The second regularization term is based on the structural binary mask to protect voxels in the regions of high susceptibility, vessels and basal ganglia structures from being over-smoothed. The mask has a zero value in the mid-brain structures and vessels. The mid-brain structures are extracted using an atlas-based segmentation method developed internally. This method segments the basal ganglia structures along with some other structures from the magnitude image, susceptibility map and enhanced T1-W image. Other high susceptibility regions such as vessels are extracted by applying a threshold to the difference of the and the low-pass filtered . This minimization problem is solved using preconditioned conjugate gradient (PCG) method. The stopping criteria for SCSWIM was based on the standard

deviation of the phase image (). The algorithm stops at the -th iteration when .

The proposed method was tested and evaluated on both simulated brain data from a 3D isotropic susceptibility model developed in (11) and in vivo MRI data acquired from a 29-year old male volunteer on a 3T Siemens scanner. This data included three double-echo STAGE scans , and . In the in vivo data, phase is unwrapped using the 3DSRNCP algorithm (12) and SHARP (13) is used to remove the background field. The reconstructed images using SCSWIM were compared to other methods such as TKD, iSWIM, and MEDI in terms of root mean squared error (RMSE) and structural similarity (SSIM) measures. The susceptibilities of different basal ganglia structures, internal cerebral vein (ICV) and straight sinus veins (SSV) The susceptibility brain model and susceptibility through multiple orientation sampling (COSMOS) (4) were used as ground truth in the simulated and in vivo data, respectively.

Results: Figure 1 (a-d) shows the structural constraint used in the SCSWIM method. The constraints derived from regular T1 and STAGE enhanced T1 are illustrated in **Figure 1(e-h).** These show that STAGE provides more information about the white and gray matter edges and it is less noisy. **Figure 2** shows the simulated model in comparison to the reconstructed susceptibility maps using TKD, iSWIM, and SCSWIM methods accompanied by the errors associated with the simulation model. Streaking artifacts are shown by red arrows. They were reduced in SCSWIM compared to TKD and iSWIM. The RMSE for TKD, iSWIM and SCSWIM were 0.014, 0.011 and 0.005 ppm, respectively. Also, the SSIM index was measured as 94.45%, 94.52% and 97.85% for TKD, iSWIM, and SCSWIM respectively. Based on these results, the SCSWIM has the lower error and higher similarity to the model compared to other methods. **Figure 3** shows the reconstructed susceptibility image using TKD (a,e,i), iSWIM (b,f,j), MEDI (c,g,k) and SCSWIM (d,h,i) methods. As can be seen in these images, SCSWIM has less noise while the sharpness of the vessels and other brain structures are well-preserved. MEDI also provides a smooth reconstruction but in the regions, that are close to the veins there are still some remaining artifacts.
In the simulated data, the susceptibility of ICV is measured as , , and ppm in TKD, iSWIM and SCSWIM compared to in the model. For the in vivo data, the susceptibility of ICV values are , , , , and for TKD, iSWIM, MEDI, SCSWIM, and COSMOS, respectively. Also, the plot in **Figure 4** shows the correlations of the measured susceptibilities in the reference image and reconstructed images using different methods for model and in vivo data. As can be seen, SCSWIM (blue color) is highly correlated with the reference image. **Figure 5** shows the parameters determined in SCSWIM based on the fidelity and regularization terms. The optimal values for SCSWIM occurred for .

Discussion: Based on the results provided in the previous section, the reconstructed image using SCSWIM has lower streaking artifacts and more accurate susceptibility values for mid-brain structures and vessels. This is mainly due to the utilization of the better contrast between grey and white matter structures provided by the STAGE data. Current implementation of SCSWIM converges at the second iteration where the inner PCG loop can go up to 60 iterations. The reconstruction is significantly accelerated compared to the SFCR algorithm.

Conclusion: In this paper, we have proposed a structural constrained-based reconstruction algorithm, SCSWIM, that employs the unique contrast of STAGE imaging and segmented deep gray matter structures and vessels to reconstruct a susceptibility map. The evaluation of SCSWIM on both simulated and in vivo human brain data shows the reliability of the geometry information, reduced streaking artifact, and accuracy of the susceptibility values of both basal ganglia and veins compared to other methods.

References

1. Haacke EM, Liu S, Buch S, Zheng W, Wu D, Ye Y. Quantitative susceptibility mapping: current status and future directions. Magnetic Resonance Imaging. 2015; 33: p. 1–25.
2. Wharton S, Schafer A, Bowtell R. Susceptibility mapping in the human brain using threshold-based k-space division. Magnetic Resonance in Medicine. 2010; 63(5): p. 1292–304.
3. Tang J, Liu S, Neelavalli J, Cheng YC, Buch S, Haacke EM. Improving susceptibility mapping using a

threshold- based k-space/image domain iterative reconstruction approach. Magn Reson Med. 2013; 69: p. 1396–407.

4. Liu T, Spincemaille P, deRochefort L, Kressler B, Wang Y. Calculation of susceptibility through multiple orientation sampling (cosmos): a method for conditioning the inverse problem from measured magnetic field map to susceptibility source image in mri. Magn Reson Med. 2009 Jan.; 61: p. 196–204.
5. Liu J, Liu T, deRochefort L, Ledoux J, Khalidov I, Chen W, et al. Morphology enabled dipole inversion for quantitative susceptibility mapping using structural consistency be- tween the magnitude image and the susceptibility mapping. NeuroImage. 2012; 59(3): p. 2560–2568.
6. Schweser F, Sommer K, Deistung A, Reichenbach JR. Quantitative susceptibility mapping for investigating subtle susceptibility variations in the human brain. NeuroImage. 2012; 62(3): p. 2083–2100.
7. Bao L, Li X, Cai C, Chen Z, van Zijl PCM. Quantitative susceptibility mapping using structural feature based collaborative reconstruction (SFCR) in the human brain. IEEE Transactions on Medical Imaging. 2016; 35(9): p. 2040–50.
8. Chen Y, Liu S, Wang Y, Kang Y, Haacke EM. Strategically acquired gradient echo (stage) imaging, part I: Creating enhanced T1 contrast and standardized susceptibility weighted imaging and quantitative susceptibility mapping. Magn Reson Imaging. 2018; 46: p. 130–139.
9. Wang Y, Chen Y, Wu D, Wang YWY, Sethi SK, Yang G, et al. Strategically acquired gradient echo (STAGE) imaging, part ii: Correcting for RF inhomogeneities in estimating T1 and proton density. Magn Reson Imaging. 2018; 46: p. 140–150.
10. Haacke EM, Reichenbach JR. Susceptibility Weighted Imaging in MRI: Basic Concepts and Clinical Applications: Wiley Blackwell; 2011.
11. Buch S, Liu S, Neelavalli J, Haacke EM. Simulated 3D brain model to study the phase behavior of brain structures. In in Proceedings of the 20th Annual Meeting of ISMRM, (Melbourne, Australia); 2012. p. 2332.
12. Abdul-Rahman HS, Gdeisat MA, Burton DR, Lalor MJ, Lilley F, Moore CJ. Fast and robust three-dimensional best path phase unwrapping algorithm. Applied Optics. 2007; 46(26).
13. Schweser F, Deistung A, Lehr BW, Reichenbach JR. Quantitative imaging of intrinsic magnetic tissue properties using MRI signal phase: An approach to in vivo brain iron metabolism? NeuroImage. 2011; 54(4): p. 2789–807.
14. Neelavalli J, Chung Y, Cheng N, Jiang J, Haacke EM. Removing background phase variations in susceptibility weighted imaging using a fast, forward-field calculation. .
15. Haacke EM, Tang J, Neelavalli J, Cheng YC. Susceptibility mapping as a means to visualize veins and quantify oxygen saturation. J Magn Reson Imaging. 201 Sep.; 32: p. 663–76.
16. Liu, J ;Liu, T;deRochefort, L; Ledoux, J; Khalidov, I;Chen, W.;Tsiouris, A. J.;Wisnieff, C;Spincemaille, P.; Prince, M. R.;Wang, Y.. Morphology enabled dipole inversion for quantitative susceptibility mapping using structural consistency be- tween the magnitude image and the susceptibility mapping," NeuroImage, vol.. 2012; 59(3): p. 2560–2568.
17. Barrett R, Berry M, Chan TF, Demmel J, Donato J, Dongarra J, et al. Templates for the solution of linear systems: Building blocks for iterative methods. SIAM. 1994.
18. Ghassaban K, Liu S, Jiang C, Haacke EM. Quantifying iron content in magnetic resonance imaging. Neuroimage. 2018.
19. Zheng W, Nichol H, Liu S, Cheng YC, Haacke EM. Measuring iron in the brain using quantitative susceptibility mapping and x-ray fluorescence imaging. NeuroImage. 2013; 78: p. 68–74.
20. Barbosa JH, Santos AC, Tumas V, Liu M, Zheng W, M. HE, et al. Quantifying brain iron deposition in patients with Parkinson's disease using quantitative susceptibility mapping, R2 and R2.*. Magnetic resonance imaging. 2015; 33(5): p. 559–565.
21. Haacke EM, Thompson MR, Brown RW, Venkatesan R. Magnetic Resonance Imaging: Physical Principles

and Sequence Design. 1999.
22. Lee CE, Baker EH, Thomasson DM. Normal regional T1 and T2 relaxation times of the brain at 3T. Proc. Intl. Soc. Mag. Reson. Med. 2006; 14.
23. Smith SM. Fast robust automated brain extraction. Human Brain Mapping. 2002 Nov.; 17(3): p. 143-155.
24. Jenkinson M, Beckmann CF, Behrens TE, Woolrich MW, Smith SM. FSL. NeuroImage. 2012; 62: p. 782-90.
25. Zhou W, Bovik AC, Sheikh HR, Simoncelli EP. Image qualifty assessment: From error visibility to structural similarity. IEEE Transactions on Image Processing. 2004; 13(4): p. 600–612.

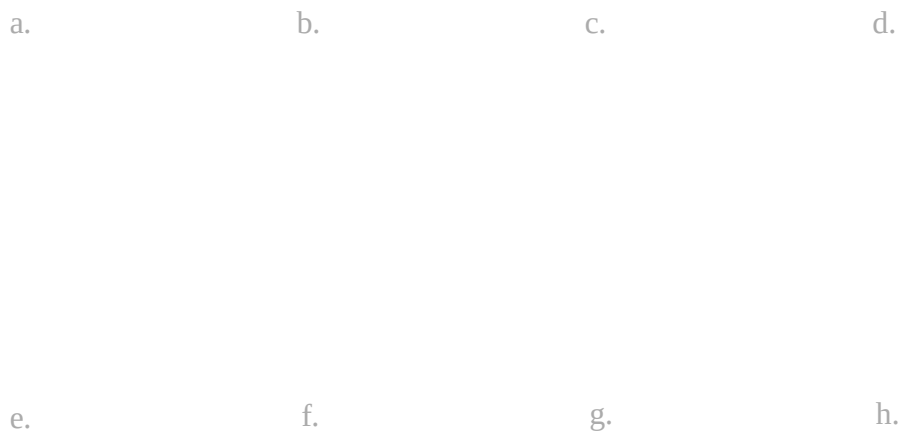

Figure 1. The first row shows the structural constraints used in SCSWIM for the in vivo data: (**a-c**) edge matrix, , in , , and directions, and (**d**) structural matrix, for the in vivo data. The second row shows the advantage of extracting constraint from the STAGE data: (**g)** T1-weighted, **(h)** STAGE enhanced T1-weighted images and the extracted edges (union of three directions) from **(f)** T1-weighted and **(g)** STAGE enhanced T1-weighted are shown. As seen **(g)** provides more information about the white and gray matter edges (shown with red arrow) and it is less noisy (regions shown with red circle) than (f).

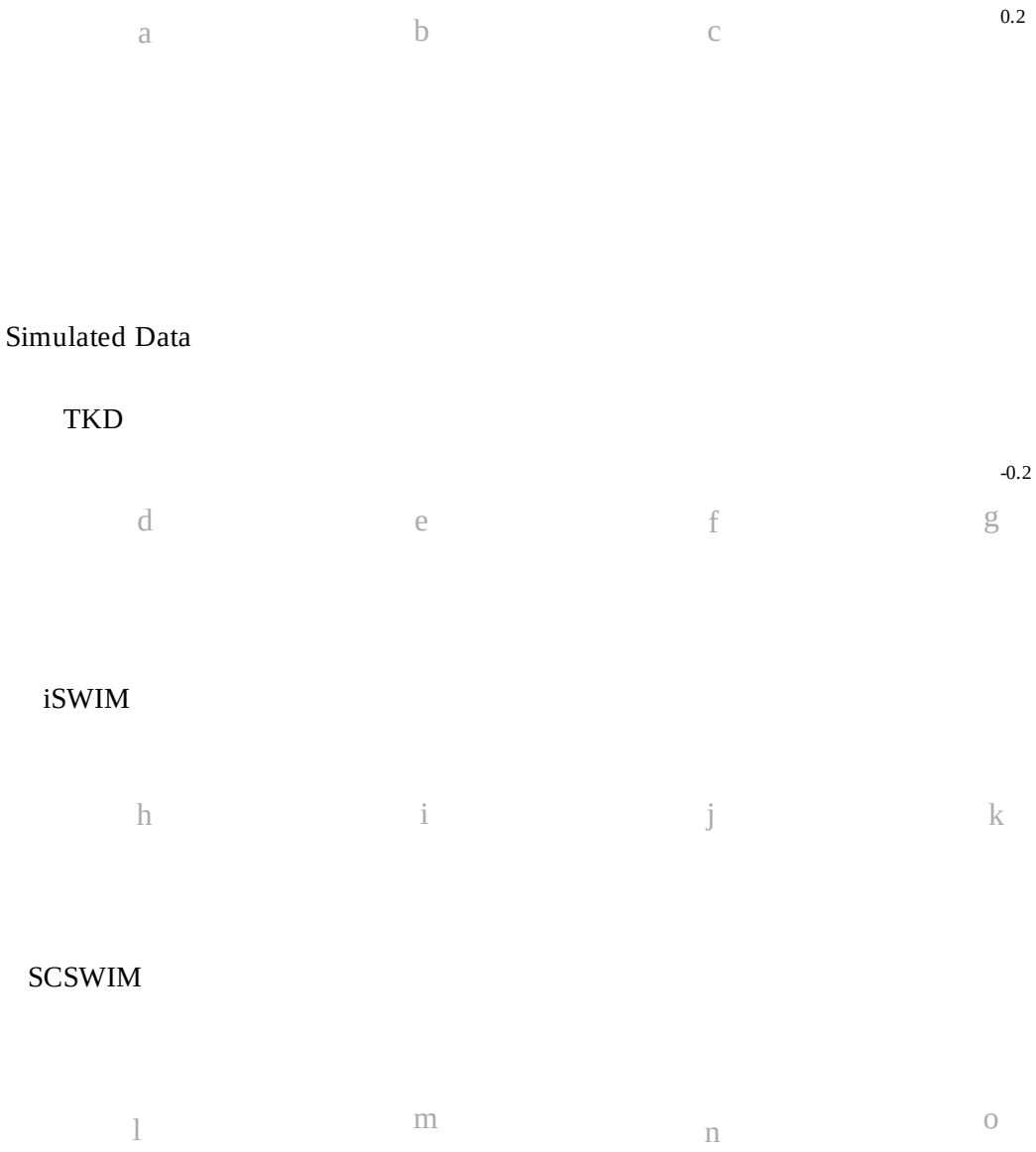

Figure 2. Axial, coronal and sagittal views of the susceptibility maps for the ideal model (**a,b,c**), TKD (**d,e,f**), iSWIM (**h,i,j**) and SCSWIM (**l,m,n**) shown in the first, second, third and fourth rows. The streaking artifacts are shown in red arrows. Also, fourth column (**g,k,o**) shows the susceptibility errors in different methods. The SCSWIM in the last row provides better reconstruction with less artifact and higher similarity to the ideal map in the first row.

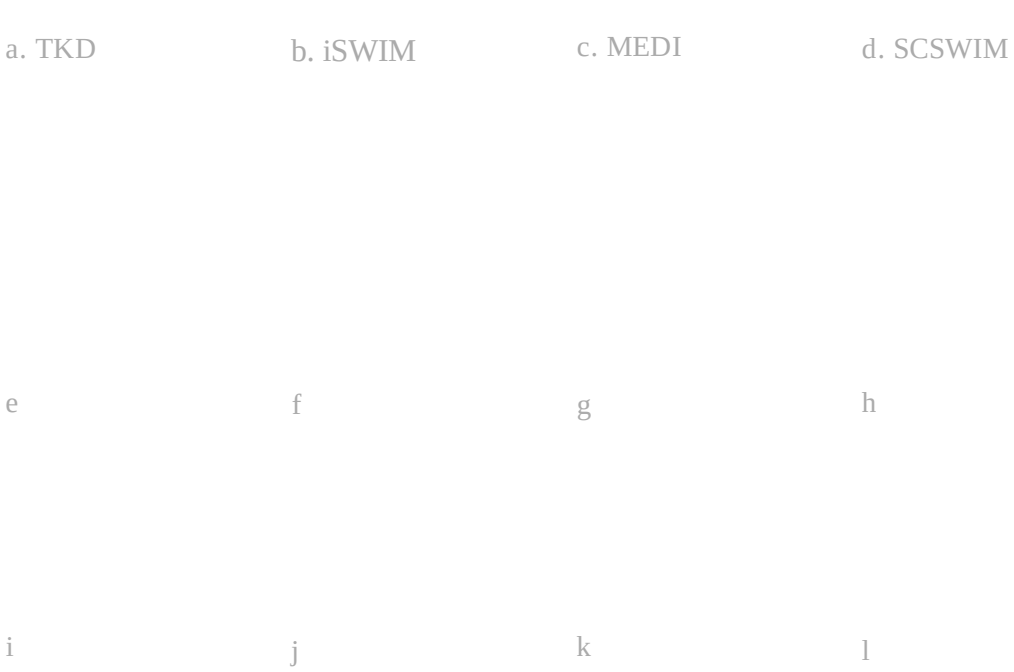

Figure 3. Susceptibility maps from TKD, iSWIM, MEDI () and SCSWIM () methods are shown in the first, second, third and fourth columns, respectively. Three orthogonal views are shown in different rows. All of the images are displayed in the same windowing level.

(a) Simulated Data

(b) In Vivo Data

Figure 4. These plots show the correlation of the deep gray matter susceptibilities in the reference image with the ones in the reconstructed images using different methods in the (a) simulated data and (b) in vivo data (TKD (black), iSWIM (green), MEDI (red) and SCSWIM (blue)). As it can be seen, SCSWIM is highly correlated with the reference image (model in the simulated data and COSMOS in the in vivo) in both plots.

(a) Determination

(b) Determination

Figure 5. SCSWIM parameter determination based on the fidelity and regulations terms. The optimal value of .